Investigation of the GCI main injection: experimental-numerical analysis of gasoline spray impact at reference engine conditions

Published Version:
Viscione, D., Mariani, V., Bianchi, G.M., Falfari, S., Ravaglioli, V., Silvagni, G., et al. (2025). Investigation of the GCI main injection: experimental-numerical analysis of gasoline spray impact at reference engine conditions. INTERNATIONAL JOURNAL OF MULTIPHASE FLOW, 182, 1-13 [10.1016/j.ijmultiphaseflow.2024.105034].

Availability:
This version is available at: https://hdl.handle.net/11585/996954 since: 2025-01-03

Published:
DOI: http://doi.org/10.1016/j.ijmultiphaseflow.2024.105034

D. Viscione, V. Mariani, G. M. Bianchi, S. Falfari, V. Ravaglioli, G. Silvagni, L. Allocca, G. Meccariello, A. Montanaro. Investigation of the GCI main injection: experimental-numerical analysis of gasoline spray impact at reference engine conditions. *International International Journal of Multiphase Flow*, Volume 182, 2025, 105034, ISSN 0301-9322,

Investigation of the GCI main injection: experimental-numerical analysis of gasoline spray impact at reference engine conditions

Abstract

This work deals with the experimental and numerical investigation of ultra-high pressure gasoline injection against heated walls in order to characterize the fuel evaporation and distribution in gasoline compression ignition combustion chambers. Spray-wall impingement tests have been conducted in a quiescent vessel and recorded by means of the Mie scattering technique. The test conditions have been set in line with those of a reference benched GCI engine, leading to 500 bar and 700 bar for the injection pressure, 298 K, 423 K, 493 K for the wall temperature, 20 mm and 30 mm for the injector-wall distance. The same test matrix has been reproduced by means of CFD three-dimensional simulations using a proper setting of the wall-impingement model and the joint use of CFD-FEM approaches for the vapour-wall heat exchange. The time evolution of the rebound spray has been recorded and then postprocessed leading to the width and the thickness of the cloud. The CFD results are in line with the experimental ones both in terms of the overall time evolution and punctual values, proving a good accuracy of the simulation in predicting the rebound/adhered fuel mass split and the local distribution of the fuel after the impingement. Given the reliability of the simulations, insights on the numerical wall film mass and evaporated mass have been provided in order to clarify the effect of increasing pressure, temperature, and distance.

1. Introduction

Framework

The rising concerns on the climate emergency and on premature deaths due to air pollution is leading to sharp changes in different technological fields. Currently, the on-road transportation sector is one of the main responsible of those worries due to the widespread of fossil fuels-based propulsion systems all over the world. Recently, the European Union members have discussed the ban of Internal Combustion Engines (ICEs) from the market within 2035 (zero carbon dioxide emission at the tailpipe). Therefore, electric batteries, fuel cells and hydrogen engines would have been the only options to power on-road vehicles. However, a u-turn, has been made, and the proposal has been significantly modified resulting in the EU7 regulations for light vehicles. EU7 is substantially a reviewed version of the EU6 including tighter limits on the particulate emission. The possibility to equip vehicles with e-fuels powered engines has been unlocked [1] since they are carbon-based synthetic fuels that can be renewably produced by combining hydrogen and carbon dioxide, resulting in a zero-net carbon emission cycle.

In this short-middle time scenario, internal combustion engines must evolve in order to fulfil the latest requirements. Implementing the so-called Low Temperature Combustion (LTC) can lead to the objective [2], being LTC based on ultra-lean combustion, which promotes the reduction of both heat losses (higher efficiency) and emissions due to the lower and more homogeneous in-cylinder temperature. In order to enhance those aspects, gasoline-like fuels have been identified as the most promising fuel option due to their higher volatility and self-ignition delay, which allow more homogeneity before the ignition [3]. Controllability, repeatability and low environmental impact of LTC operations require the split of the gasoline injection into two or three events at ultra-high injection pressure [4] (from 500 bar up to thousands bar) in order to smoothly set the distribution of both fuel and temperature to achieve the proper start and sustain of combustion. An example of one of the most promising LTC technology is the Gen 3X Gasoline Compression Ignition (GCI) engine developed by Delphi Technologies [5] equipped on a middle-class passenger vehicle for testing. The Authors have shown the potential of this engine to achieve 48% brake thermal efficiency at different operation points while ensuring low NOx and acceptable soot emission, proving the ability to overperform some reference hybrid ICE-battery vehicles. This result has been achieved by adopting a fast air heating line, a tailored valvetrain and advanced turbocharging as well as an optimized combination of combustion chamber (at compression ratio 17) and injection system called 'wetless combustion system'. In particular, the 'wetless' system aims at minimizing the wetting of the in-cylinder surfaces (mainly piston and liner), which is a major shortcoming for the engine emissions. Indeed, the spray wall wetting hampers the fuel energy conversion quality [6] [7] [8] by inducing the local cooldown of the mixture, which leads to: i) longer ignition-delay time; ii) increased amount of unburnt hydrocarbons; iii) increased soot formation.

In GCI engines, the likelihood of wall wetting is enhanced by the need to phase the main injection (in which the largest amount of the gasoline is introduced into the cylinder to ensure the required brake energy) near the top dead centre. Therefore, investigating the spray-wall wetting at ultra-high injection pressure and high wall temperature is mandatory for pushing this technology towards the marketplace. The gasoline fuel spray behaviour has been studied in a plethora of literature works, both experimental and computational ones. However, the most recent studies can be divided into two main research branches: i) the gasoline free-spray behaviour, mainly testing different ambient pressure and injection pressure values, including GCI-consistent ones, e.g. 2-40 bar for the ambient pressure, 500-2000 bar for the injection pressure [3] [7] [8] [9] [10] [11] [12] [13]; ii) the gasoline spray-wall impingement, mainly testing high temperature values of the surface, representative of those of the engine piston during combustion [6] [7] [14] [15] [16], but adopting injection pressure values between 50 and 200 bar.

Contribution

To the best knowledge of the authors, the current state of the art lacks investigations on the combined effect of ultra-high gasoline injection pressure and hot wall. One of the most comprehensive works in the literature, is the one proposed by Peraza et al. [7] in which the fuel is injected up to 1500 bar against a wall heated up to 550 K in an experimental facility that then allowed the combustion of the mixture. Optical analyses by means of Schlieren and chemiluminescence techniques have been used in order to provide insights on the spray impact behaviour and the ignition delay time. However, neither the use of gasoline (the test fuel was n-dodecane) nor the use of a synergic experimental-numerical approach have been presented.

In the opinion of the Authors, the state of the art should be enriched by results, both experimental and numerical, describing the behaviour of gasoline-like fuels at ultra-high injection pressure against hot walls. At this set of conditions, new results can guide the interpretation of existing experimental measurements as well as the early design step in the field of GCI engines, in which the combustion features are strongly affected by the three-dimensional local fuel distribution.

In this work, both experimental and numerical analyses have been conducted on gasoline spray wall-impingement injected at ultra-high pressure (up to 700 bar) against an hot plate surface (temperature up to 493 K). The single-hole gasoline injector has been positioned at two different distance sets from the plate (20 mm and 30 mm). In the experimental analysis, the MIE scattering optical technique has been used to capture the morphology of the rebound spray cloud, then, the width (radial penetration) and the thickness (axial penetration) of the cloud have been detected on the images. The numerical analysis has been focused on the validation of the experimental campaign with three-dimensional Computational Fluid Dynamics (CFD) simulations. The results have been compared in order to assess the ability of the simulation to reproduce the fuel distribution driven by ultra-high injection pressure gasoline at engine heat up conditions. A Matlab algorithm has been developed and tested in order to provide a fair comparison between experimental and simulation images. Once the reliability of the simulation setting has been proven, additional numerical results have been presented in the perspective of engine CFD simulations.

This experimental-numerical work has been driven by the need of insights on the gasoline spray rebound and wall film formation during the main injection event in a reference GCI bench engine [17] [18]. The choice of the test matrix has been guided by the need to understand the spray impact phenomena that determine the stability or not of some operating points of the reference GCI engine. The aim of the authors is to contribute to extend the knowledge on gasoline-like sprays wall impingement at boundary conditions that have been scarcely investigated at now, providing helpful results for GCI mixing assessment.

2. Experimental method

The experimental apparatus and the analysis methodology for a time-space detailed characterization of the wall impingement on a flat wall is described in this section. The tests have been performed in an optically accessible vessel through three wide quartz windows allowing to collect the images. A low surface-roughness aluminum wall (1.077 μm average roughness) has been installed inside the vessel, flat in shape and orthogonally disposed with respect to the fuel propagation. The wall has been electrically heated and controlled in temperature by a J-type thin thermocouple located at the center 1.0 mm under the surface. The plate has been heated at 423 K and 493 K. Two different nozzle-tip wall distances (*d*) have been tested i.e., 20 mm and 30 mm. Two injection pressure values have been tested, namely 500 bar and 700 bar, leading to the mass flow rate profiles shown in Figure 1.

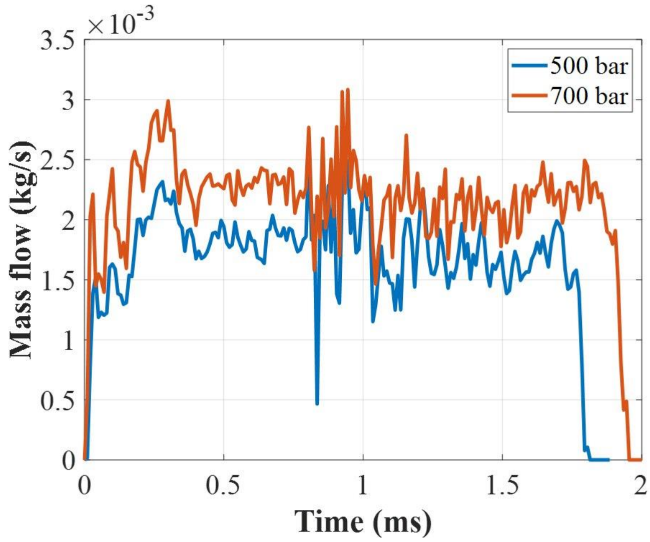

Figure 1: Mass flow rate profile of the single hole injection device for two test pressures.

Pump commercial gasoline (main properties listed in Table 1) has been adopted as a fuel, kept at the constant temperature of 297 K and injected by a single-hole CR diesel device.

Table 1: Experimental points

Fuel property	Gasoline
Formula	C4 to C12
Molecular weight (g/mol)	100–105
Carbon (mass%)	85-88
Hydrogen (mass%)	12-15
Oxygen (mass%)	2,7
Aromatic content (%v/v)	35
Density @15 °C (kg/L)	0,72–0,775
Boiling point (°C)	27–225
Vapor pressure @38 °C (kPa)	48–103
Specific heat (kJ/kg/K)	2
Viscosity @20 °C (mPa s)	0,37–0,44
LHV(MJ/L)	30–33
Autoignition temperature (°C)	257
RON/MON	98/87
(RON+MON)/2	92,5
Cetane	5-20
Flammability limit (vol %)	1,4/7,6
Water Tolerance (vol %)	Negligible
Stoichiometric air/fuel	14,7
Sulphur (mg/kg)	10

The behavior of the fuel during the free-evolving phase, the wall-impingement and the spreading has been analyzed by collecting images using a time-resolved optical techniques. The Mie-scattering methodology has been adopted. A high-power flash lamp, synchronized with the injection command, enlightened the spray from the right side while a high-speed C-Mos camera collected and stored the evolution phases for an off-line analysis. A sketch of the optical setup is reported in Figure 2 where the lamp illuminated the incoming spray while a Z-type arrangement branch collected the figures of the phenomenon at a high-speed rate. The Z-configuration of the apparatus in Figure 2 enables a higher spatial resolution with respect to a direct system.

The high intensity litght passes through the front window and lights up the liquid part of the injected jet. The light scattered by the liquid spray impacts an 15° off-axis parabolic mirror (4 inches in diameter, 500 mm parent focal length) and deflected onto a 200 mm focal length that focuses the light beam on the high-speed camera. The chosen distance between the nozzle and the plate filled only partially the 80 mm test vessel section (defined through the quartz window) so an acquiring matrix on the camera of 960x288 pixels was set with a frame speed of 14,400 frames per second (fps) for the 20 mm as distance case. While for the 30 mm case, a spatial resolution of 896x416 pixels was set with a frame rate of 10,800 fps.

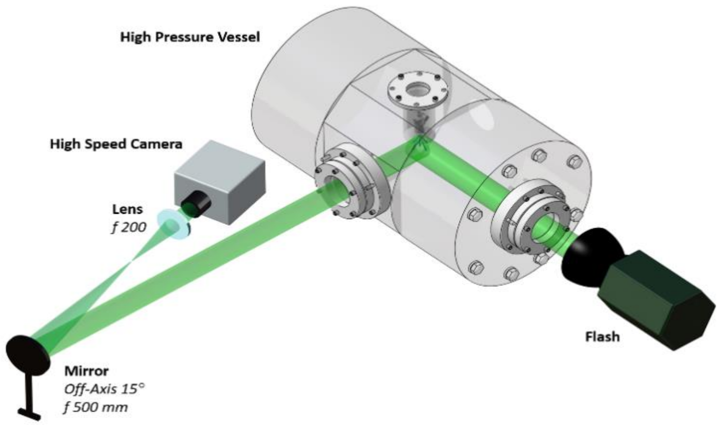

Figure 2: Optical setup for the Mie-scattering image acquisitions.

In Figure 3 an example of a typical image derived from the application of the described technique, is reported. Due to its axial-symmetry, half impingement is enough for the event description so realizing resource saving. The fuel hits the flat wall and spreads on its surface realizing dynamic complex figures of the rebounded cloud that, in a row approximation, can be described as width and thickness parameters. The first one captures the slipping of the fuel on the wall, far from the impingement point while, the second one captures the rebound of the spray orthogonally to the surface. The image-collecting device was a Fastcam SA4 high-speed camera synchronized with the injection command and realizing two time-resolutions, 92.6 and 69.4 µs, were obtained for the 30.0 mm and 20.0 mm tip-wall distances, respectively. The spatial calibration factor was 12.1 pixel/mm. Five consecutive shots have been carried out to obtain an evaluation of the jet spreads on the measurements. More details concerning the application of the optical technique are reported in [19].

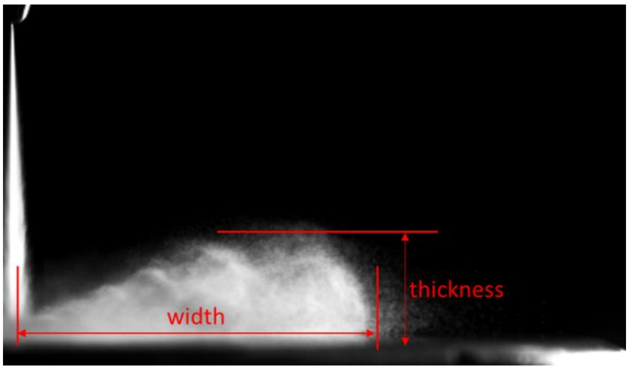

Figure 3: Typical image of fuel showing the parameters of interest in the impact.

A cycle-resolved sequence of images is reported in Figure 4. The figure reports the incipient impingement of the jet in the first frame that, typically, is indicated as t_0. Then, the fuel starts slipping along the surface while first appearances of fluid-dynamic interactions with the gas (N_2) in the vessel appear. Then, the rebound becomes more significant (third and fourth frames) showing, on the top of the image, the classical curls born by the interaction with the gas.

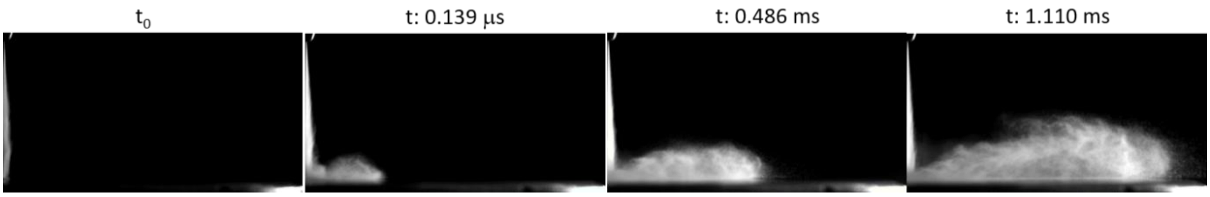

Figure 4: Cycle-resolved sequence of images taken at p_{inj}: 700 bar, T_{wall}: 293 K, d: 20 mm.

The Mie-scattering images were treated through a customized algorithm developed in C# to extract the parameters of interest. Mainly, the net ambient (to better outline the contours of the liquid), and the extract contour of the rebound shapes were used to obtain the width and thickness parameters. Once identified the image, an automated procedure applied on all the image sequences determined the mean values and the standard errors. Background subtraction, gamma correction, morphology filtering, levels linear, gaussian blur, and threshold filtering, as such as the fill hole operation have been applied on the Mie-scattering images to enhance the jet figures. Eventually, contour detection allowed identifying their boundaries. A batch method extracted the width and thickness as a function of the ambient pressure and wall temperature. A detailed description of the processing is reported in [20], [21]. The complete experimental test matrix is reported in Table 2

Table 2: Experimental test points

Distance (mm)	Injection pressure (bar)	Plate temperature (K)
20	500	298 – 423 – 493
	700	
30	500	
	700	

3. Numerical method

Computational mesh

The CFD simulations have been performed with the commercial software STAR-CD v4.28. The computational domain is shaped as a squared box with base dimensions of 80 mm x 80 mm and height adjusted according to the injector tip-wall simulation test (20 mm or 30 mm). In particular, once the tip-wall distance has been chosen, the height of the box has been set to 28 mm and 40 mm, respectively. The height-coordinate adjustment is needed in order to prevent interaction between the newly generated parcels and the top wall boundary. Figure 5 shows the section view of half the computational grid, highlighting the refinement features.

The base grid size has been set to 4 mm in the regions in which, based on the experimental images, the droplets should not be present. The grid is refined up to 1 mm in the expected rebound spray region. Eventually, the grid is further refined up to 0.5 mm and then 0.025 mm along 8 mm and 4 mm downstream the nozzle tip in order to capture the spray atomization and break-up. With this setup, the number of cells was 148120 in the 20 mm tests, and 157127 in the 30 mm tests.

On the side boundaries, a pressure boundary condition has been imposed with fixed pressure (1 bar) and temperature (298 K). The top and the bottom boundaries have been treated as walls with fixed temperature: i) 298 K for the top wall; ii) the test temperature (298 K, 423 K, 493 K) for the bottom wall.

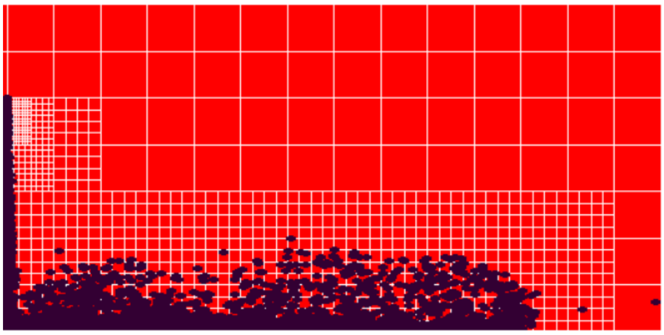

Figure 5: Section view of the computational grid (tip-wall distance 20 mm) with simulated spray overlap.

In order to capture the spray-wall impingement properly, the bottom wall has been coupled with the STAR-CD built-in one-dimensional Conjugate-Heat Transfer (CHT), which solves the equations of the conductive and convective heat transfer according to the Finite Element Method (FEM) approach. In this way, the temperature of each cell face on the bottom wall is updated according to the heat flux exchanged between the fluid phase (mainly the adhered fuel liquid wall film) and the solid phase. Figure 6 gives a graphical view of the model. Once the wall on which the model should be applied is identified (Conjugate heat transfer interface) a chosen number of layers (i) is used to discretize the solid height. For each layer, the heat transfer equations are computed. In correspondence of the bulk dept (B), the temperature is not affected by the heat exchange, thus, it has been set at the test temperature as a constant value. For the present study, a bulk dept of 0.5 mm has been imposed.

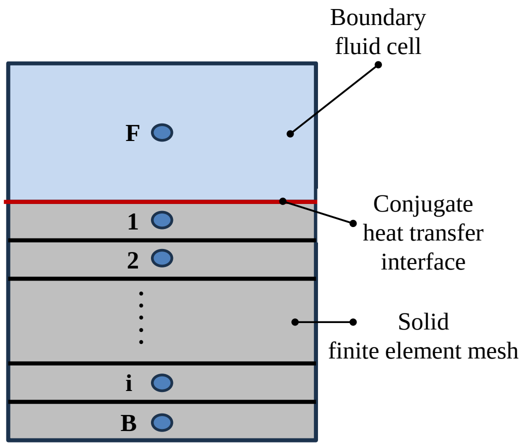

Figure 6: Scheme of the implementation of the 1D-CHT model.

The implementation of this model adds accuracy in the final results, as the characteristics of the scatter against the wall are affected by the expected local cooling of the plate at the fuel liquid film formation sites.

Determination of the Leidenfrost and Nukiyama temperatures

In the case of a liquid that hit a heated wall, the evaporation rate increases as the wall temperature increases. This behaviour is consistent up to the so-called Nukiyama temperature (T_N) which promotes the transition boiling regime i.e., an evaporation rate reduction. This is due to the generation of an insulating layer made of the vapor phase of the liquid upon the hot wall, which reduces the conductive heat transfer. When the vapour layer has reached a consistent and fully developed structure, the evaporation rate is minimum, since the direct liquid-wall contact is prevented (Leidenfrost effect). This occurs at the Leidenfrost temperature (T_L). The further heating-up of the wall over the Leidenfrost temperature results in the classical evaporation rate increase.

A proper estimation of the Leidenfrost and Nukiyama temperatures is a key for accurate predictions at high-temperature wall wetting conditions. At ambient pressure, the determination of the Leidenfrost temperature is only related to the nature of the liquid. In fact, in case of finished surfaces [22], the surface roughness has a poor influence on the post-impinged behaviour. Moreover, the diameter of the impinging droplet (5 μm) is well above the measured surface roughness (around 1 μm). In the current study, the authors selected a pseudo-pure liquid from the NIST database that is representative of the characteristics of the commercial Gasoline. In particular, the critical pressure and critical temperature declared in the database are 25.7 bar and 544 K, respectively.

The Leidenfrost temperature can be calculated by means of the Spiegler model [23] (27/32 T_{CR}), which is reliable for ambient pressure (1 bar in this study) well below the critical pressure of the liquid. As a result, the Leidenfrost temperature of the gasoline-like pseudo-pure liquid is 459 K. Moving on the determination of the Nukiyama temperature, in the case of lack of experimental data, the 'middle-point' approximation is a common practice, namely, the Nukiyama temperature is calculated as the middle temperature between the Leidenfrost one and the saturation one at ambient conditions (Eq. (1)). Being 371 K the value of the equilibrium temperature at 1 bar from the STAR-CD built-in database, the resulting value of the Nukiyama temperature is 415 K.

$$T_{N,@1\,bar} = \frac{T_{SAT,@1\,bar} + T_{L,@1\,bar}}{2} \tag{1}$$

Droplet-wall interaction model

In this study, the STAR-CD custom Bai-ONERA model has been adopted [24], [25] mainly due to its ability to account for high-temperature contact phenomena with a smooth transition between natural convection and nucleate boiling regimes, which are not standard features in wall-impingement modelling.

The behaviour of a parcel that hits a wall mainly depends on the wall temperature and on the parcel kinetics. The first one is parametrized by the non-dimensional temperature T^* (Eq. (2)), which relates the temperature of the wall (T_w) with the Leidenfrost effect. The second parameter is parametrized by the Sommerfeld number (Eq. (3)), a combination of the Weber and Ohnesorge numbers.

$$T^* = \frac{T_w - T_N}{T_L - T_N} \tag{2}$$

$$K = We\ Oh^{-0.4} = \left(\frac{\rho D v^2}{\sigma}\right)\left(\frac{\mu}{\sqrt{\rho \sigma D}}\right)^{-0.4} \tag{3}$$

In Eq. (3) ρ, D, v, σ, μ are density, diameter, velocity, surface tension and viscosity of the incoming liquid droplets. From Eq. (3) it is visible that the Sommerfeld number is strongly affected by the parcel velocity, which is mainly given by the injection pressure. As the gasoline injection pressure adopted in this study is well above the standard ones, there is lack of data to check the resulting Sommerfeld number at these velocities.

Figure 7 shows the map of the impingement regimes adopted in the Bai-ONERA model (based on iso-octane tests) depending on the T^* and K values. At $T_w = T_N$ ($T^* = 0$), the maximum heat flux is reached. This point on the Bai-ONERA map identifies the upper boundary of the *nucleate boiling* regime (blue straight line between deposition and splash). At $T_w = T_L$ ($T^* = 1$), the minimum heat flux is reached. This point identifies the *transition boiling* regime (intersection between blue and red curves). For $T_w > T_N$ ($T^* > 1$), the heat flux increases again. This condition is called *film boiling* regime and it is identified by the straight red line between rebound and splash.

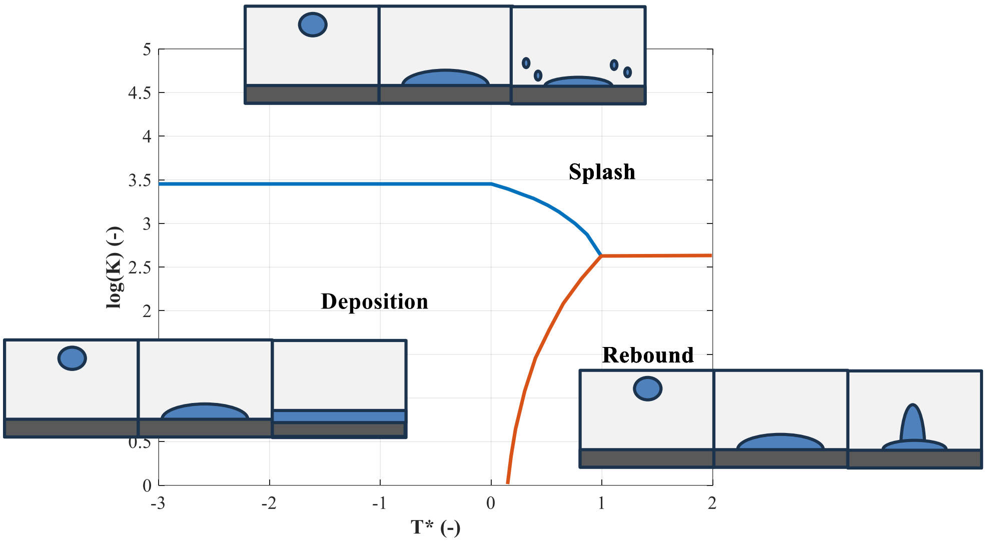

Figure 7: Map of the Bai-ONERA model showing the different impacting regimes.

The data on the incoming droplets needed to calculate the Sommerfeld number depends on the development of the free spray along the path between the injector tip and the heated plate. The free spray is simulated according to a coupled Eulerian-Lagrangian approach, and the parcels are introduced inside the computational domain by imposing the injection profile (mass-flow rate versus time) provided by the experimental measurements. In particular, the set of models to predict the free spray before the impact is resumed in Table . The O'Rourke model [26] for the collision has been used to increase the accuracy of the simulated scatter as it allows to account for coalescence, separation, bouncing, and momentum transfer between droplets. The full description of the free spray model, setting and validation has been given in a previous work [12], and it is not reported in this paper for the sake of brevity.

Table 2: models adopted for the CFD setup

Phenomenon	**Model**
Turbulence	RANS k-epsilon RNG
Atomization	Huh and Gosman [27]
Breakup	Reitz-Diwakar [28]
Inter-droplet collision	O'Rourke [26]
Drag	Schiller and Naumann [29]
Evaporation	El Wakil [30]

Image postprocessing methodology

In order to extract width and thickness of the rebound cloud from simulation images, a dedicated postprocessing algorithm has been developed in Matlab. It is underlined that in CFD practice the dispersed phase is tracked by ‘parcels’, namely Lagrangian entities that are representative of a statistical sample of droplets. As a result, in order to limit the computation time, a single parcel represents a number of droplets. Thus, the simulated spray, being populated by parcels, is less dense than the real spray. In this framework, the algorithm used to process the experimental images based on the intensity of the lighted cloud (which depends on the droplets population), would be ineffective. On the other hand, identifying width and thickness as the coordinates of the furthest parcel and the highest parcels respectively, can be misleading. Indeed, sporadic parcels inconsistent with the rebound cloud figure may be present. In order to perform a fair comparative analysis between experiment and simulation, two different regions of the CFD spray have been recorded: the rebound core spray, and the rebound dispersed spray. The rebound core spray is the denser region of the rebounded cloud, while the rebound dispersed spray is the wider region comprising dispersed parcels if they are clustered in small groups (sporadic parcels with no neighbours will be not taken into account). A droplet has a neighbour if at least one additional droplet is present in any direction in a distance of 1-2 mm.
Thus, the limits of the core spray are identified as the first point at which one droplet has not any neighbour above (for the thickness) and at the right (for the width). Conversely, the dispersed spray region is identified as the rectangle comprising all the rebounded droplets.
An example of this this processing criterion is summarised in Figure 8. Once the algorithm has recognized the rebound core spray (red region) and the rebound dispersed spray (blue region), their base dimensions (length and height) are converted to distances from the injector axis, resulting in the simulation width and thickness.

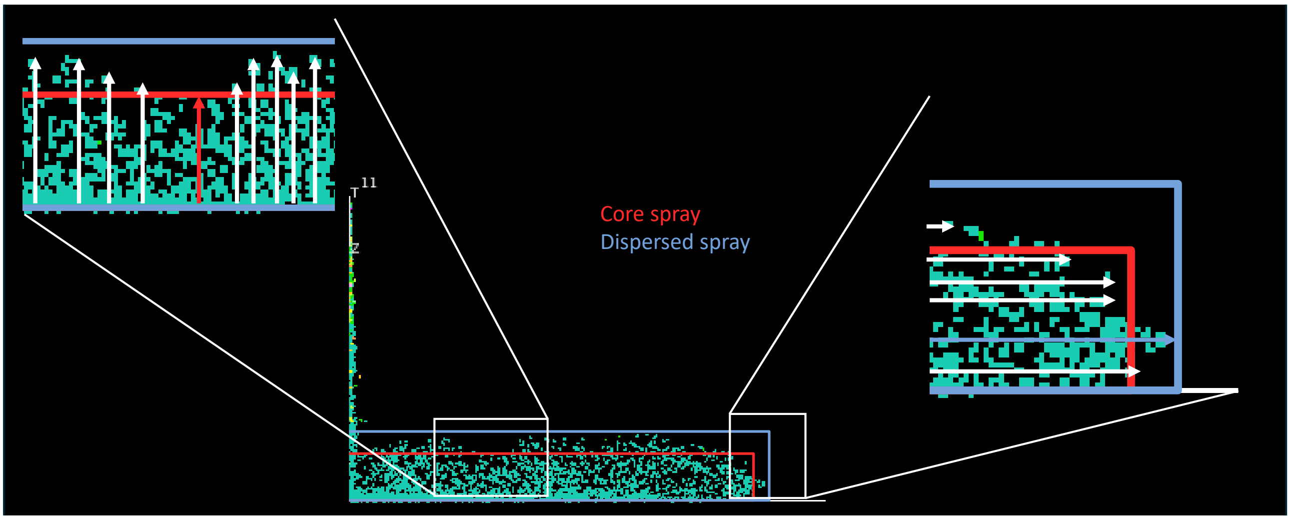

Figure 8: Comparison between the core and dispersed simulated spray regions.

4. Results

In this section the results obtained from the simulations are compared with the ones provided by the experimental campaign. Firstly, the analysis of the impingement dynamics will be presented by describing the position of the impinging parcels on the Bai-ONERA model map. Then, the validation of the methodology will be made by comparing width and thickness of the rebound cloud as well as the overall spray morphology.

For each injector-plate distance (20 mm, 30 mm) and injection pressure (500 bar, 700 bar), three different plate temperatures have been considered: 298 K, 423 K and 493 K. The first one represents a reference base condition, at which the plate has not been heated. The other two temperatures have been selected according to the calculated T_N and T_L: 423 K is higher than T_N = 415 K, while 493 K is higher than T_L = 459 K. In this way, all the three different impact regimes have been investigated. The choice of these temperatures has been done also in the view of capturing the fuel impinging behaviour in typical engine operations [31].

Bai-ONERA maps

In order to capture the key characteristics of the impinging parcels, a dedicated user sub-routine has been implemented. In particular, at each time-step the sub-routine selects the parcels which are about to hit the wall i.e., parcels that fall in the last fluid cell (1 mm upon the wall), then, the algorithm averages all the characteristics that are then used to compute the Sommerfeld number (Eq. (3)). Therefore, the simulation allows to analyse the time-evolution of the impinging parcels kinetics at given wall temperature.

Figure 9 reports the Sommerfeld number evolution of the incoming parcels as markers at 500 bar and 20 mm distance. Each group of markers in a row is given by one simulation at initial wall temperature T^*, whilst the color of the marker identifies the recording instant. For the first and the third groups of markers, the non-dimensional temperature is almost constant during the simulation around the initial value (markers lies on straight lines), meaning that the amount of the adhered fuel leads to low heat transfer. Considering the third group, this trend is consistent with the hypothesis of the creation of a thin vapour film, which decreases the heat flux between the liquid film and the heated plate. Considering the first group, the heat flux can be neglected as well, since the wall surface and the liquid spray have the same temperature (around 298 K). A slightly higher misalignment of the markers, representative of wall temperature variation during injection time, is reported for the second group of markers. Since the non-dimensional wall temperature is close to zero, the heat transfer is close to the maximum value.

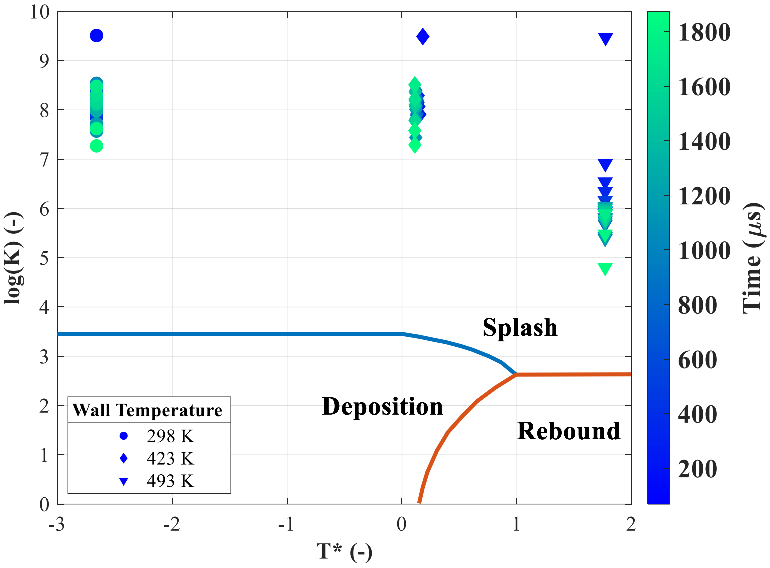

Figure 9: Points on the Bai-ONERA map for the injection pressure of 500 bar and distance of 20 mm.

Figure 10 shows the same trends for the higher injection pressure (700 bar). Also in this case, the condition inside the transition boiling regime leads to a higher heat transfer between the heated plate and the liquid film (markers misalign). In both Figure 9 and 10, the Sommerfeld number has an oscillating trend. In fact, analysing the curves of the injected mass flowrate (Figure 1), their shape is highly irregular. Overall, once the injection is about to stop, the mass flow rate decreases causing a reduction of the droplet velocity. As a result, at the end of injection, the Sommerfeld number decreases as well. Furthermore, it is visible that regardless of the injection pressure and non-dimensional temperature, the fate of the impinging parcels will be the splash. Thus, the larger part of the impinging fuel mass is scattered in the form of child parcels with smaller diameter, whilst the remaining fuel mass adheres upon the wall. This is also confirmed by analysing the trend of velocity and mean diameter of the impinging parcels shown in Figure 11-a and Figure 11-b, respectively.

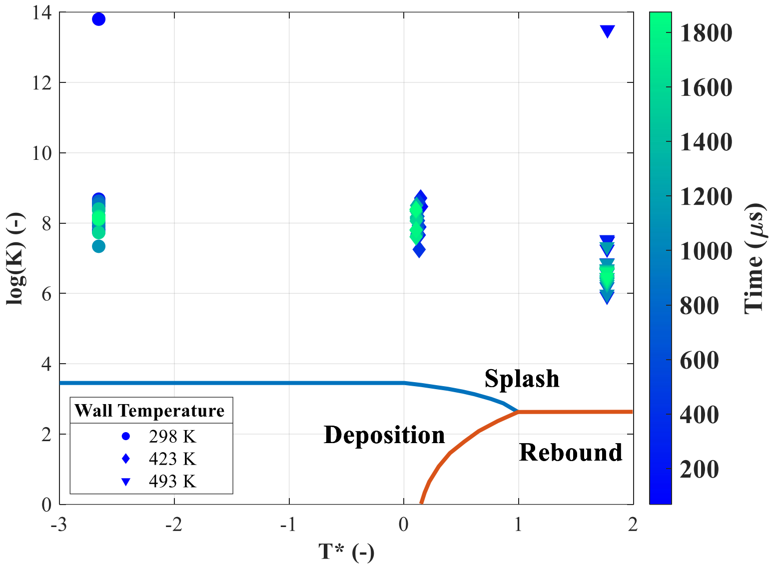

Figure 10: Points on the Bai-ONERA map for the injection pressure of 700 bar and distance of 20 mm.

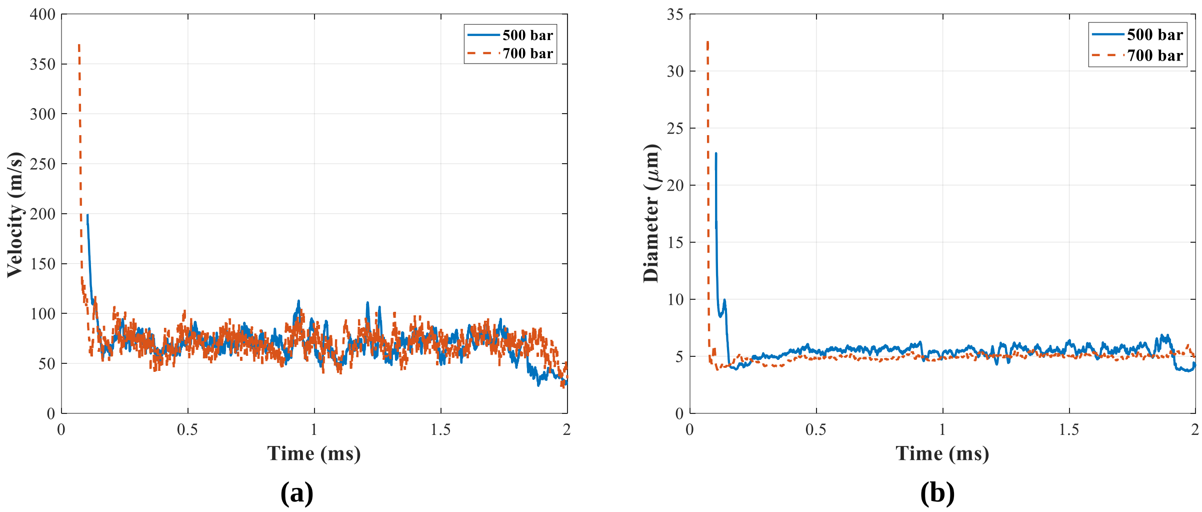

Figure 11: Velocity and diameter for both injection pressures, distance of 20 mm, and wall temperature at 423 K.

Figure 11 shows that both the velocity and diameter are almost the same for the two injection pressures investigated. In particular, the curves of the velocity fluctuate due to the fluctuating nature of the fuel mass flow rate, causing the Sommerfeld to be irregular as well. Regarding the other test conditions, Appendix A shows the Bai-ONERA maps for the distance 30 mm. The overall aspect of the map is the same as that at 20 mm distance. Markers associated at late impingement time (green) are more dispersed and associated to lower values of the Sommerfeld number. This is due to the longer distance (30 mm) that promotes the aerodynamic drag effect on the impinging parcels, resulting in lower velocity and diameter.

Width and thickness

In this section, width and thickness of the simulated and experimental rebound clouds are compared. As anticipated in Section 2, simulation results are included between the curve of the core spray (red) and that of the dispersed spray (blue). Experimental results (black lines) report both the average behaviour and the confidence bars. The bars represent the range between the maximum and minimum values obtained during the 5 five consecutive shots.

Figure 12 shows the results obtained by the tests performed at a distance of 20 mm and the injection pressure of 500 bar. Concerning the width (left column), it is visible that the experimental overall time-evolution of the radial penetration is well captured by the core-dispersed including area.

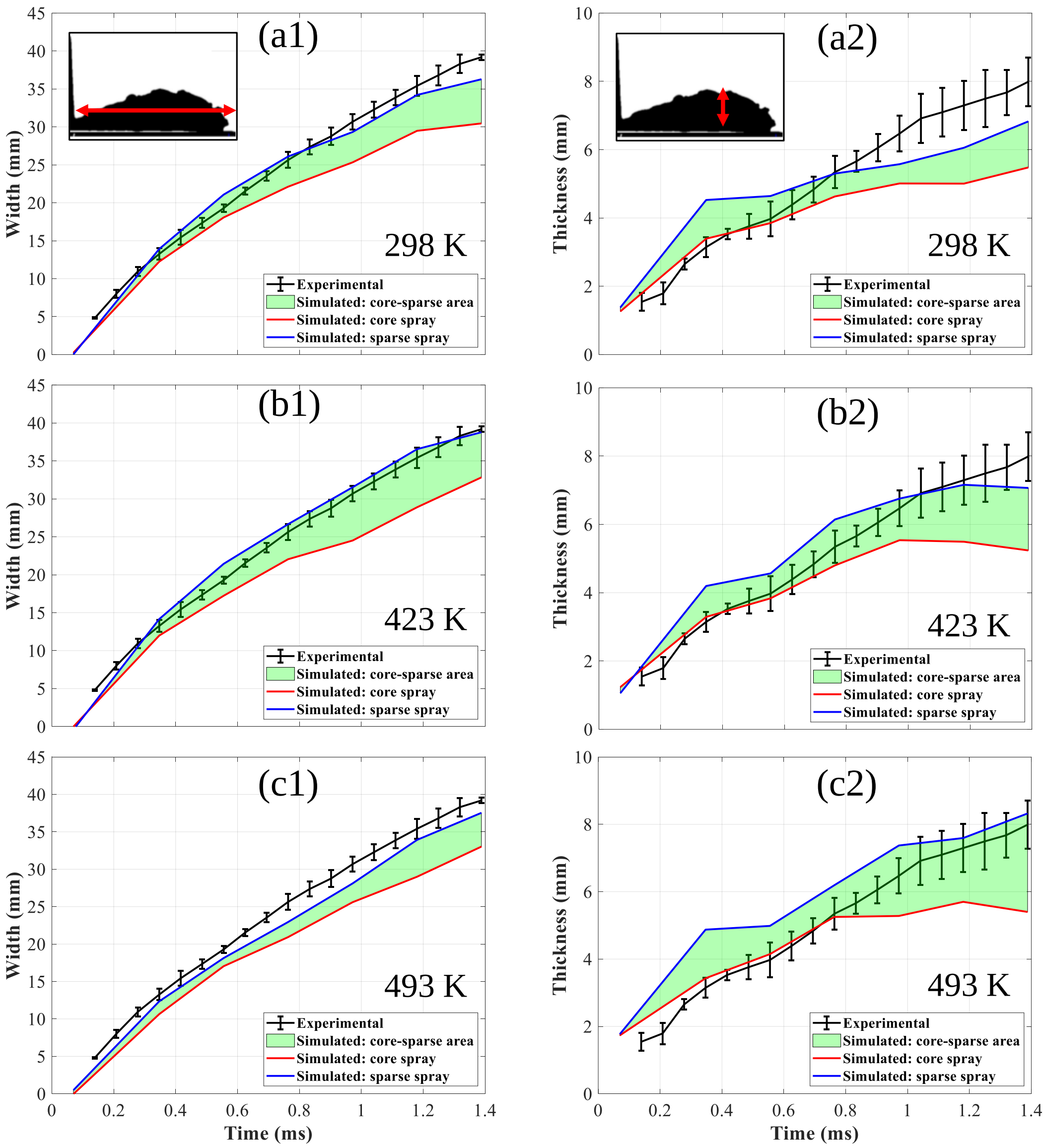

Figure 12: Comparison between width and thickness of the rebounded cloud for a distance of 20 mm between the injector tip and the heated plate and an injection pressure of 500 bar (a1 and b1: 298 K; b1 and b2: 423 K; c1 and c2: 493 K).

The core width (red) underestimates the penetration during all the simulation, whilst the dispersed width (blue) is in line with the experimental values. A slight underestimation can be seen for the secondary cloud width at the highest wall temperature (Figure 12-c1). Focusing on the right column, the simulated core-dispersed including area becomes wider along the injection event. This is due to the different behaviour of the core thickness (red), which quickly flattens up, and that of the dispersed thickness (blue), which instead moves upward according to the experimental curve. Figure 12-a2, 12-b2, 12-c2 shows that the simulation accuracy improves as the temperature of the plate increases, indeed the experimental curve at 493 K fully lies in the including area, while a slight underestimation is observed at 423 K and 293 K. This could be be expected, since the Bai-ONERA model has special features to capture the post-impingement characteristics in the case of hot walls. It is underlined that the accuracy loss at lower plate temperature values occurs moving towards the end of the simulation time. This trend, as will be explained later, deals with the generation of vortexes due to the interaction between post-impinged parcels and air.

Figure 13 shows the same curves for the higher injection pressure (700 bar). As seen for 500 bar, the experimental width of the scattered cloud (left column) is well reproduced in both overall behaviour and punctual values. Regarding the thickness (right column), the same observations presented for Figure 12 can be recalled. However, the accuracy loss towards the advanced phase of the injection at 700 bar is more significant than that at 500 bar, thus, it is enhanced at higher spray velocity. Furthermore, the value at which the simulation curves flatten is almost the same over the different tests (6-8 mm).

A computational three-dimensional analysis of the motion inside the vessel reveals that the simulation thickness underestimation is likely due to the lack of a vortex that should blow the impinged droplets away from the impact point, rolling them up resulting in an increased axial penetration. Figure 14 compares the simulated vector field relative to the velocity with the shape of the experimental rebound cloud. The white solid line on the left side represents the contour of the simulated cloud. Observing the relative position of the vortex compared to the contour of the cloud in the simulated case, the point at which the maximum thickness is located, is almost above the axis of the vortex. This is reasonable since the droplets around the vortex's axis receive a grater energy from the air momentum. Instead, at the periphery, the magnitude of the velocity vector is almost zero, causing the cloud to flatten. As a result, the code is able to capture the intensity and location of the vortexes, but their dissipation time is shorter compared to the experiment, thus, they cannot blow those parcels neither towards the periphery, nor up enough compared to the expectations.

The same considerations can be done to the cases related to a greater distance between the injector tip and the heated plate (30 mm). More details can be found in Appendix B. The experimental-numerical comparison shown in Appendix B is in line with that presented in this section, however the including area between core and dispersed at 30 mm is slightly tighter. This is due to the larger aerodynamic drag along the longer parcel free path through the air medium. During this longer path most of the parcels have reached the stable diameter, thus, the resulting spray is finer and more homogeneous.

Comparing all the measurements between experiments and simulations, the curves corresponding to the dispersed spray are more representative of the real scatter spray motion. The present methodology can suit the simulation of the main injection event in GCI engines (high piston temperature, high gasoline injection pressure, short injector-piston distance) and provide reliable information on the after-impingement liquid fuel distribution and evaporation. Data to check out directly the reproduction of the liquid film would be beneficial to completely validate the code in predicting a GCI combustion process.

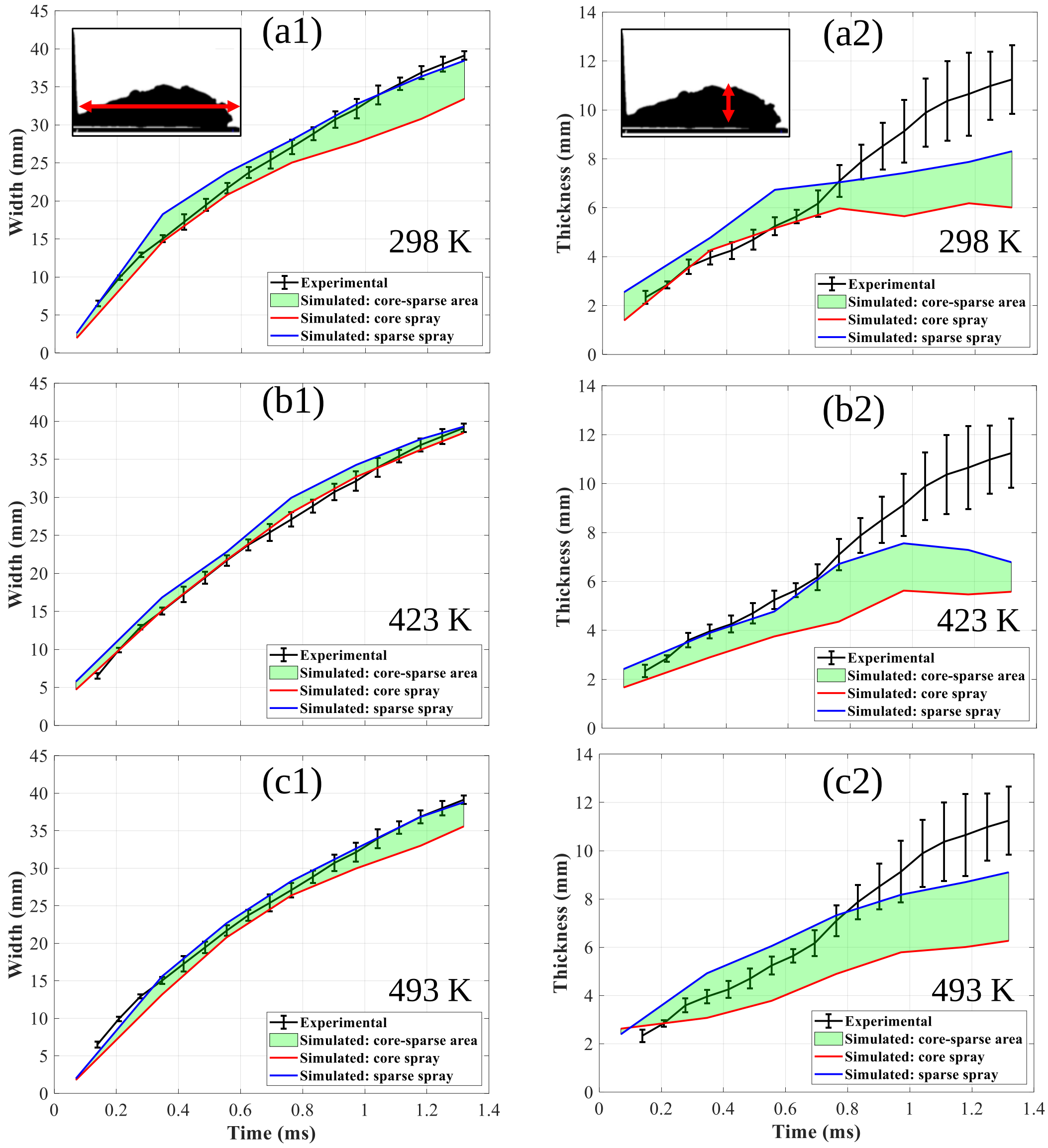

Figure 13: Comparison between width and thickness of the rebounded cloud for a distance of 20 mm between the injector tip and the heated plate and an injection pressure of 700 bar (a1 and b1: 298 K; b1 and b2: 423 K; c1 and c2: 493 K).

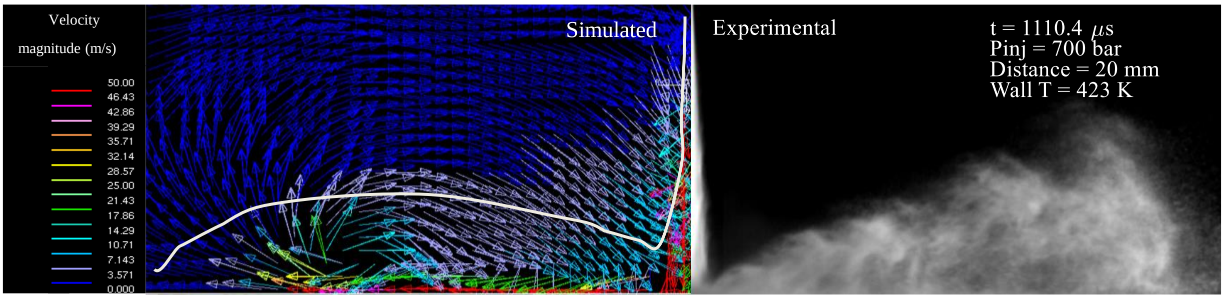

Figure 14: Comparison between the experimental spray morphology and the simulated vector field of velocity during the steady-state phase for the injection pressure of 700 bar, distance of 20 mm, and wall temperature at 423 K.

Spray morphology

In this section, the analysis the whole spray morphology will be performed. The comparison will be made pointing to the most noticeable characteristics highlighted in the previous section.

In Figure 15 simulation (left side) and experimental (right side) images are compared at the very early spray-wall impingement (almost free spray condition). Simulation images show the Lagrangian parcels coloured by diameter values while experimental images show the liquid dispersed phase thanks to the Mie scattering. The agreement between the jet development in the two images is a sign that the liquid length penetration is the same. Thus, the simulation very early impingement conditions (timing and footprint) can be considered reliable.

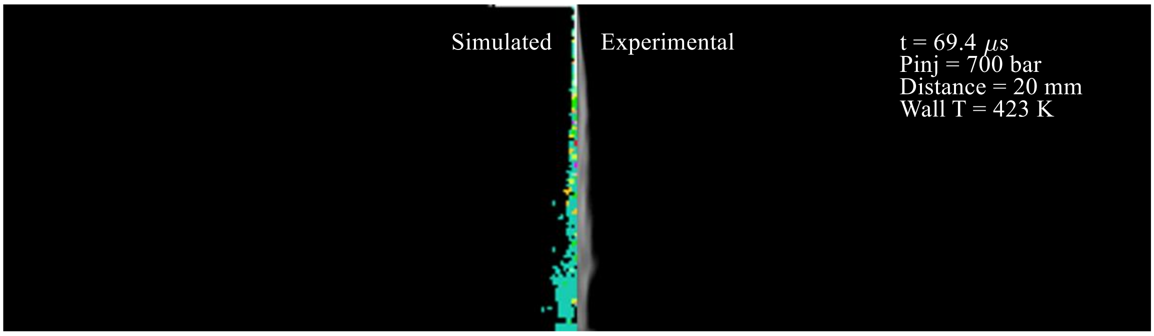

Figure 15: Comparison between the spray morphology during the early injection development for the injection pressure of 700 bar, distance of 20 mm, and wall temperature at 423 K.

Figure 16 shows the morphology comparison at the end of the needle opening transient at 700 bar injection pressure, 20 mm tip-wall distance, 423 K wall temperature. As also reported in Figure 13, at $t = 0.62\,ms$ both the width and thickness of the simulated cloud fit the experimental measurements. The experimental image of Figure 16 reports two main vortexes that strain the rebound cloud. These vortexes are promoted by the momentum transfer from the secondary jet (squeezed between the free jet and the wall) to the air. As previously mentioned, the evolution of the vortex highlighted in red is responsible for the offset between the experimental and simulated thickness at the late stage of the injection. As a result, the simulation cloud moves towards the radial direction flattening up to a uniform thickness along the axial direction.

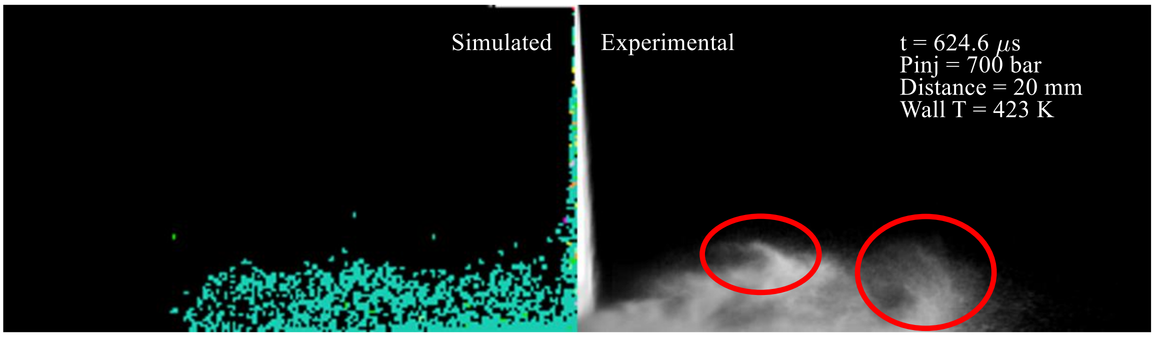

Figure 16: Comparison between the spray morphology during the early stage of the steady-state phase for the injection pressure of 700 bar, distance of 20 mm, and wall temperature at 423 K.

Figure 17 shows the morphology comparison during the steady state phase of the injection. It is visible that the simulated thickness is lower than the experimental one, while the widths are consistent between each other's. It is worth mentioning that the scatter angle in the simulation ($\theta_{sim} = 12°$) is lower than the one in the real case ($\theta_{exp} = 19°$), owing to a flatter shape of the cloud. The mismatch between the experimental and simulated clouds might be attributed to the lack of possibility to properly tune the constants of atomization and break-up models. In fact, given the limited acquisition frequency of the camera, only one image of the free spray has been recorded. The adoption of a multi-component surrogate that better represent the properties of commercial gasoline might be an additional improvement of the simulation outputs since the dynamic properties will be affected accordingly.

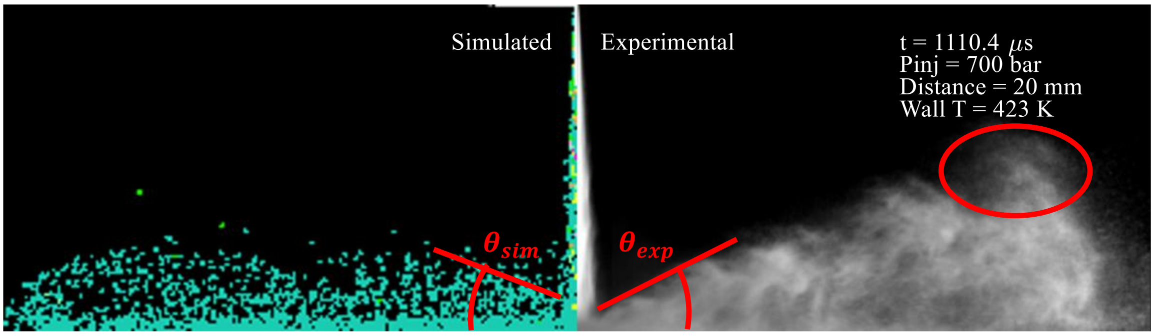

Figure 17: Comparison between the spray morphology during the steady-state phase for the injection pressure of 700 bar, distance of 20 mm, and wall temperature at 423 K.

For a lower injection pressure, the thickness of the simulated cloud follows the one of the experiments. Figure 18 compares the spray morphology obtained by imposing an injection pressure of 500 bar and a distance of 30 mm. For the same record time of Figure 17 (around 1110 μs), the morphology of the simulated cloud is similar to the experimental one, especially considering the values of width and thickness. The similarity between the values of thickness is due to the generation of almost the same angle of the reflected droplets, i.e. $\theta_{sim} = 8°$ and $\theta_{exp} = 10°$. For this case, Figure 19 shows a comparison between the velocity vector field of the simulated injection and the experimental spray morphology.

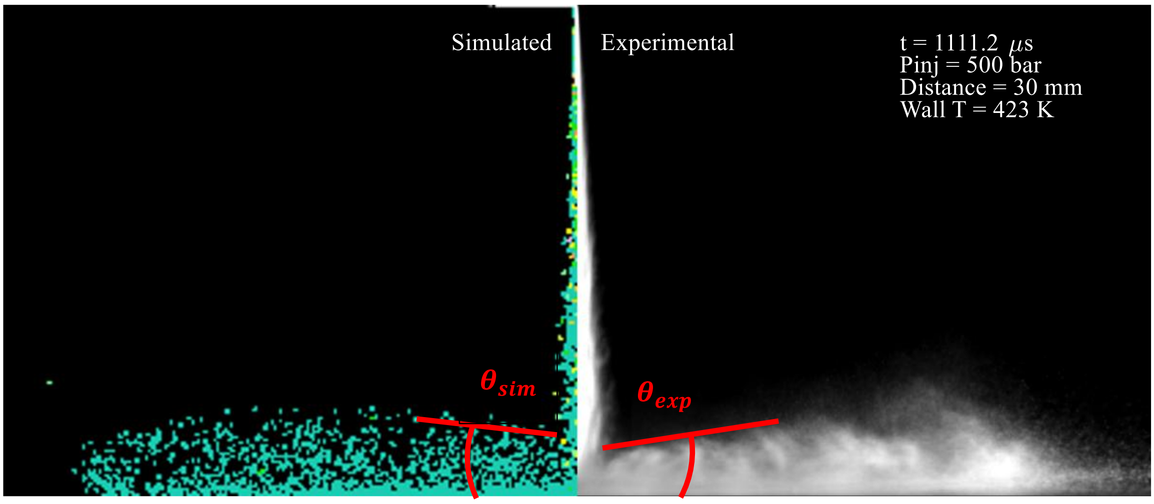

Figure 18: Comparison between the spray morphology during the steady-state phase for the injection pressure of 500 bar, distance of 30 mm, and wall temperature at 423 K.

In Figure 19 the location of the maximum thickness corresponds to the point at which the vortex is generated. In this case, the location of the maximum thickness is in good agreement with the experimental one highlighted by the red ellipse. As a result of the realistic vortex generation, the match of the overall shape of rebounded cloud is significantly improved.

The combination of longer distance of 30 mm and the reduced injection pressure of 500 bar leads to the generation of a weaker vortex as well, as the vector magnitude demonstrates. In fact, the magnitude of the vertical velocity vectors for the case shown in Figure 14 and Figure 19 are almost 14 and 20 m/s, respectively. A more intense vortex allows the cloud to develop in the vertical direction. The magnitude of the velocity vectors at the periphery of the cloud are the same for both the conditions (20 mm and 30 mm), leading the width to approach almost the same values (almost 40 mm) regardless of the distance.

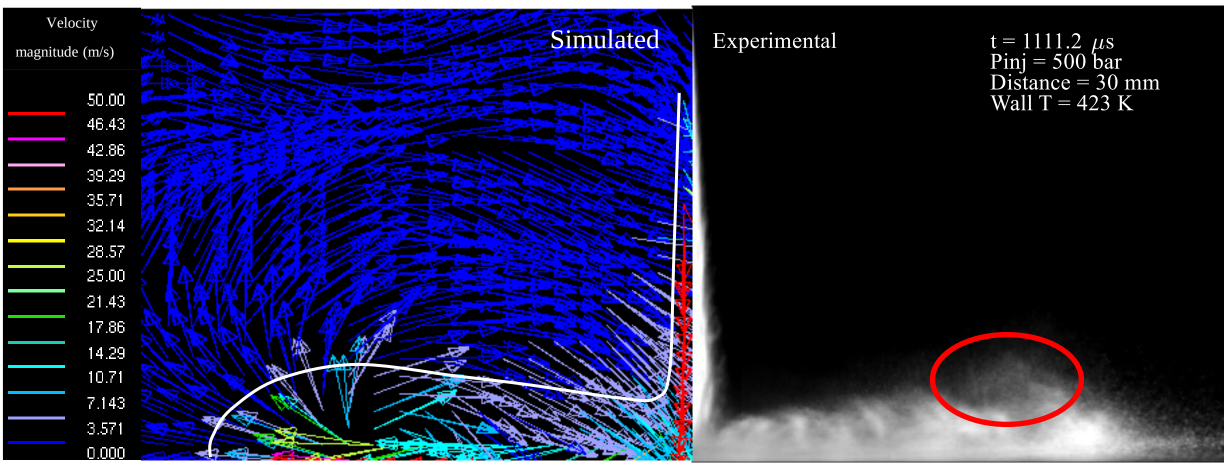

Figure 19: Comparison between the experimental spray morphology and the simulated vector field of velocity during the steady-state phase for the injection pressure of 700 bar, distance of 30 mm, and wall temperature at 423 K.

Analysis of the liquid film

In this section, the simulated time evolution of injected mass, film mass and dispersed fuel mass are compared in the view of giving further explanations to the trends shown above. Figure 20 gives a comparison for the case at 20 mm varying the injection pressure and normalizing the different masses with the total amount of injected fuel.

According to Figure 20-a1 and 20-a2, the amount of generated liquid film is strongly dependent on the plate temperature. As expected, the larger mass of fuel wall film is generated at 298 K, since no evaporation from the heat exchange with the plate occurs. Instead, for the higher two temperatures, the Leidenfrost effect comes into play. At 493 K no wall film mass is generated due to the insulating vapour layer created. Hence, all the injected fuel is in the form of dispersed parcels or vapour (Figure 20-b1,20-c1 and 20-b2, 20-c2).

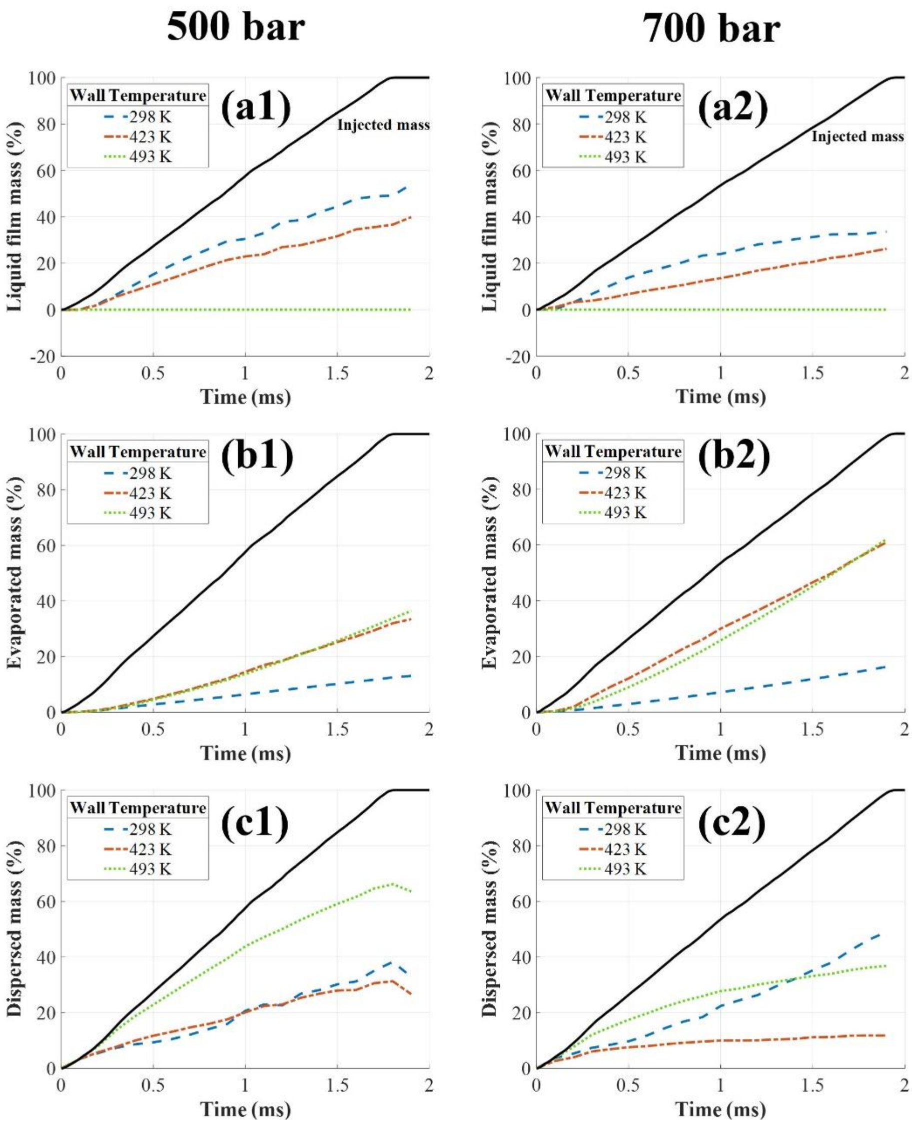

Figure 20: Comparison of the trends of liquid film (a1, a2), evaporated (b1, b2) and dispersed masses (c1, c2) for the distance of 20 mm between the injector and the plate.

The higher injection pressure of 700 bar promotes a faster evaporation of the fuel mass (Figure 20-b1, 20-b2). This is due to the higher atomization rate, which leads to slightly smaller mean diameter of the impinging parcels with respect to the case at 500 bar (Figure 11b). Therefore, a larger surface is involved in the heat transfer, owing to the fuel mass to evaporate quickly. The effect of the faster atomization is reflected on a reduced amount of dispersed mass (Figure 20-c1 and 20-c2), which identifies the morphology of the rebounded cloud. In conclusion, the discrepancy between the experimental and numerical thickness of the rebounded cloud for the cases at 700 can be also attributed to a reduced amount of dispersed fuel, that mitigates the momentum transfer between the parcels and, consequently, the upward motion of the cloud after the impingement. Same considerations applied to the case at 30 mm distance (Appendix C). It is highlighted that in Figure C1-b1, Figure C1-b2, Figure C1-c1, Figure C1-c2 is visible that at 30 mm the evaporated mass percentage is larger than that at 20 mm due to the enhanced phase change and parcels diameter reduction along the longer free path.

5. Conclusions

This work if focused on the investigation of gasoline spray impingement against heated wall at ultra-high injection pressure. The final aim of the work is providing insights on the behaviour of gasoline fuel spray after the impingement at non-conventional injection condition. The work can enrich the knowledge on the fuel distribution produced by the main injection event in modern Gasoline Compression Ignition engines.

The investigation has been conducted both with experimental tests and numerical CFD simulations on a matrix including 12 points comprehensive of: i) two injection pressure values (500 bar and 700 bar, consistently with the values operated on a reference benched GCI engine); ii) three temperature sets of the heated wall (298 K, 423 K, 493 K); two distance sets of the injector tip from the impact wall (20 mm, 30 mm). Those values have been chosen as representative of the piston bowl temperature at low, mid, and high load, and of the injector tip-piston distance during the main injection event. During the experimental tests, images of the rebound spray cloud have been captured via Mie scattering technique. Then, the images have been processed to determine the radial penetration (width) and the axial rebound height (thickness) of the cloud.

Both experiments and simulations show the following features: i) the rebound width is not significantly affected neither from the injection pressure, nor by the plate temperature, showing a monotonous increasing shape along the injection time; ii) the cloud width is strongly affected by the injection pressure and by the distance. The higher is the injection pressure, the higher is the rebound height of the spray according to an increasing behaviour. The higher is the distance, the more the width shape approaches a flat height since half of the injection time, likely due to larger spray momentum losses during the longer free spray path.

Possible reasons for the mismatch of experimental and simulation measurements might be attributed to the lack of possibility of fine-tuning the constants of atomization and break-up models. Tuning the models based only on one image due to the limited acquisition frequency of the camera, limits the accuracy in predicting velocity and diameter distributions of the impinging parcels. Standard simulation practice on coupling the Eulerian turbulence dispersion and the Lagrangian dispersed parcels likely limits the accuracy of the rebound thickness prediction, due to the small number of droplets per parcels set in order to save computation time. Improvement should be tested (e.g., the mesh grading near the periphery of the impingement point) in order to account for a more realistic momentum exchange between air and dense sprays at ultra-high injection pressure without losing computation speed.

According to CFD results, differences in the mass split in the test cases are mainly due to the wall temperature are and the distance. At 493 K no liquid fuel film is formed consistently with the lack of direct contact between the spray and the wall due to the Leidenfrost effect. At 423 K and 493 K the mass of fuel vapor is very similar, however, the case at 493 K is characterized by a larger amount of fuel mass in the form of rebound droplets that can affect the features of the diffusive combustion phase. A longer distance (30 mm) allows a larger conversion of the liquid fuel mass to fuel vapour leading to a smaller presence of fuels in the form of droplets or liquid film.

References

1. https://climate.ec.europa.eu/eu-action/transport/road-transport-reducing-co2-emissions-vehicles/co2-emission-performance-standards-cars-and-vans_en, accessed 18/09/2024

2. Krishnamoorthi, M., Malayalamurthi, R., et al., A review on low temperature combustion engines: performance, combustion and emission characteristics, *Renew. Sustain. Energy Rev.*, 116, 2019, https://doi.org/10.1016/j.rser.2019.109404

3. Feng, L., Sun, X., et al., Gasoline spray characteristics using a high pressure common rail diesel injection system by the method of laser induced exciplex fluorescence, *Fuel*, 302, 2021, https://doi.org/10.1016/j.fuel.2021.121174

4. Peer, J., Backes, F., et al., Development of high turbulence, low particle number, high injection pressure gasoline direct injection combustion system, *SAE Int. J. Engines*, 9(4), 20216, 10.4271/2016-01-9046

5. Sellnau, M., Foster, M., et al., Pathway to 50% brake thermal efficiency using gasoline direct injection compression ignition, *SAE Int. J. Adv. & Curr. Prac. in Mobility*, 1(4), 2019, 10.4271/2019-01-1154

6. Nouri, J., Whitelaw, J., Impingement of high pressure gasoline sprays on angled surfaces, *At. Sprays*, 16, 2006, 10.1615/AtomizSpr.v16.i6.70

7. Peraza, J. E., Payiri, R., et al., Analysis of spray/wall impingement using an ECN single-hole injector and a controlled-temperature wall under realistic engine conditions, *Appl. Therm. Eng.*, 208, 2022, 10.1016/j.applthermaleng.2022.118167

8. Kim, D., Shin, J., et al., Characteristics of in-cylinder flow and mixture formation in a high-pressure spray-guided gasoline direct-injection optically accessible engine using PIV measurements and CFD, *Energy Convers. Manag.*, 248, 2021, 10.1016/j.enconman.2020.112865

9. Ullal, A., Lehnert, B., et al., Experimental study of high-pressure reacting and non-reacting sprays for various gasoline blends, *SAE Int. J. Fuels Lubr.*, 17(2), 2024, 10.4271/04-17-02-0009

10. Lehnert, B., Conrad, C., Wensing, M., GDI sprays with up to 200 MPa fuel pressure and comparison of diesel-like and gasoline-like injector designs, *SAE Tech. Paper*, 2020, 10.4271/2020-01-2104

11. Wadekar, S., Yamaguchi, A., Oevermann, M., Large-eddy simulation study of ultra-high fuel injection pressure on gasoline sprays, *Flow Turbul. Combust.*, 107, 2020, 10.1007/s10494-020-00231-0

12. Viscione, D., Mariani, V., et al., Unconventional gasoline spray injection events: compared evolution of experimental data and numerical simulations, *Fuel*, 355, 2024, https://doi.org/10.1016/j.fuel.2023.129438

13. Montanaro, A., Allocca, L., Meccariello, G., Effects of ultra-high injection pressures up to 100 MPa on gasoline spray morphology, *SAE Tech. Paper*, 2020, 10.4271/2020-01-0320

14. Muddapur, A., Sahu, S., et al., Spray-wall impingement in a multi-hole GDI injector for split injection at elevated wall temperature and ambient conditions, *Therm. Sci. Eng. Prog.*, 33, 2022, https://doi.org/10.1016/j.tsep.2022.101367

15. Montanaro, A., Allocca, L., et al., Impinging jets of fuel on a heated surface: effects of wall temperature and injection conditions, *SAE Tech. Paper*, 2016, https://doi.org/10.4271/2016-01-0863

16. Kobayashi, Y., Zama, Y., Kuboyama, T., Modeling wall film formation and vaporization of a gasoline surrogate fuel, *Int. J. Heat Mass Transf.*, 147, 2020, 10.1016/j.ijheatmasstransfer.2019.119035

17. Ravaglioli, V., Ponti, F., et al., Performance assessment of gasoline PPC in a light-duty CI engine, *SAE Tech. Paper*, 2022, https://doi.org/10.4271/2022-01-0456

18. Stola, F., Ravaglioli, V., et al., Injection pattern investigation, for gasoline partially premixed combustion analysis, *SAE Tech. Paper*, 2019, https://doi.org/10.4271/2019-24-0112

19. Montanaro, A., Allocca, L., Lazzaro, M., Iso-octane spray from a GDI multi-hole injector under non- and flash boiling conditions, presented at the *International Powertrains, Fuels & Lubricants Meeting*, Oct. 2017, pp. 2017-01–2319, 10.4271/2017-01-2319

20. Allocca, L., Montanaro, A., et al., Under expanded gaseous jets characterization for application in direct injection engines: experimental and numerical approach, presented at the *WCX SAE World Congress Experience*, Apr. 2020, pp. 2020-01–0325, 10.4271/2020-01-0325

21. Otsu, N., A Threshold Selection Method from Gray-Level Histograms, *IEEE Trans. Syst. Man Cybern.*, 9(1), 1979, 10.1109/TSMC.1979.4310076

22. R. Lindagren, I. Denbratt, R. Lindagren, and I. Denbratt, ‘Influence of Wall Properties on the Characteristics of a Gasoline Spray After Wall Impingement’, presented at the 2004 SAE Fuels & Lubricants Meeting & Exhibition, SAE International, Jun. 2004. doi: 10.4271/2004-01-1951

23. P. Spiegler, J. Hopenfeld, M. Silberberg, C. F. Bumpus, and A. Norman, ‘Onset of stable film boiling and the foam limit’, *Int. J. Heat Mass Transf.*, vol. 6, no. 11, pp. 987–989, Nov. 1963, doi: 10.1016/0017-9310(63)90053-X

24. C. Bai and A. D. Gosman, ‘Development of Methodology for Spray Impingement Simulation’, presented at the International Congress & Exposition, Feb. 1995, p. 950283. doi: 10.4271/950283

25. G. Rosa, P. Villedieu, D. J., and G. Lavergne, ‘A new droplet-wall interaction model’, 2008

26. P. J. O’Rourke, ‘Collective Drop Effects in Vaporizing Liquid Sprays’, PhD thesis, Princeton University, 1981

27. K. Y. Huh and Gosman, A.D., ‘A phenomenological model of diesel spray atomization’, in *Proc. the International Conf. on Multiphase Flows, 1991*, Tsukuba, 1991

28. R. D. Reitz and R. Diwakar, ‘Effect of Drop Breakup on Fuel Sprays’, presented at the SAE International Congress and Exposition, Feb. 1986, p. 860469. doi: 10.4271/860469

29. L. Shiller and A. Naumann, ‘A drag coefficient correlation’, presented at the VDI Zeitung, 1935. doi: 77:318–320

30. M. Wakil, O. Uyehara, and P. Myers, ‘A theoretical investigation of the heating-up period of injected fuel droplets vaporizing in air’, presented at the NACA Technical Note 3179, May 1954

31. D. Mayer, A. Seelig, T. Kunz, F. Kopple, M. Mansbart, and M. Bargende, ‘Experimental Investigation of Flame-Wall-Impingement and Near-Wall Combustion on the Piston Temperature of a Diesel Engine Using Instantaneous Surface Temperature Measurements’, in *SAE 2018 International Powertrains, Fuels and Lubricants Meeting, FFL 2018, September 17, 2018 - September 19, 2018*, in SAE Technical Papers, vol. 2018- September. Heidelberg, Germany: SAE International, 2018. doi: 10.4271/2018-01-1782

Appendix A

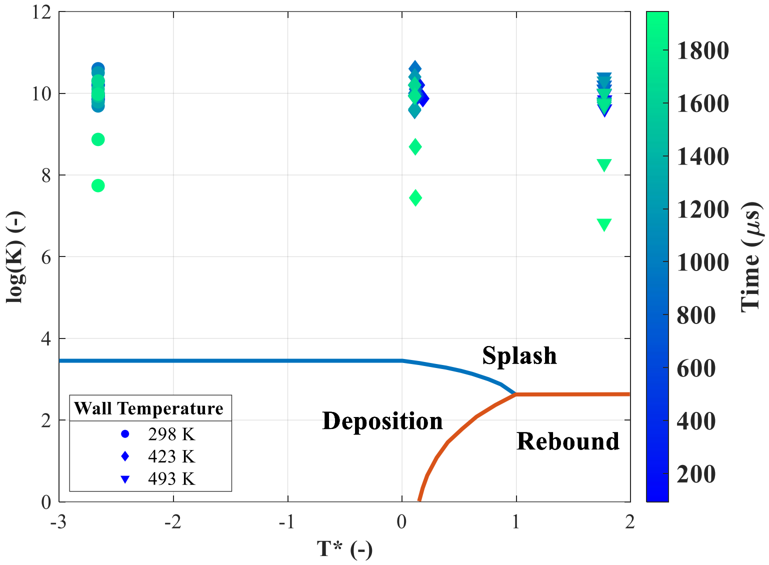

Figure A-1: Points on the Bai-ONERA map for the injection pressure of 500 bar and distance of 30 mm.

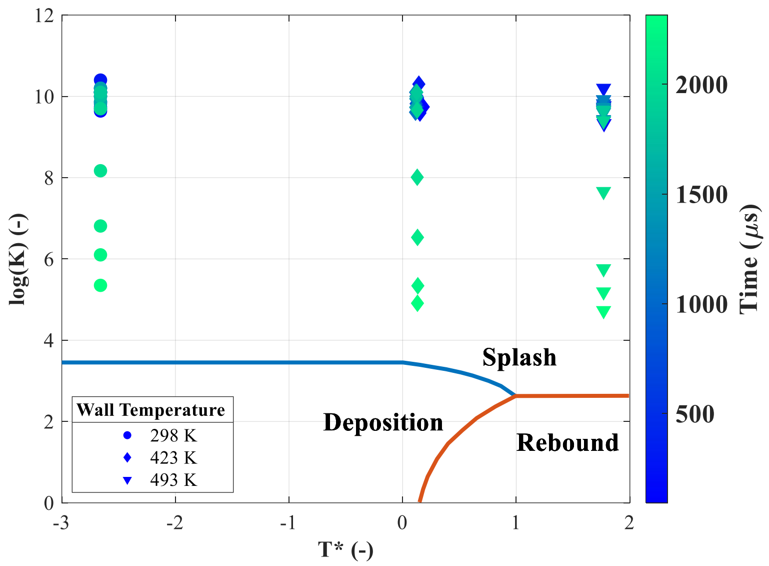

Figure A-2: Points on the Bai-ONERA map for the injection pressure of 700 bar and distance of 30 mm.

Appendix B

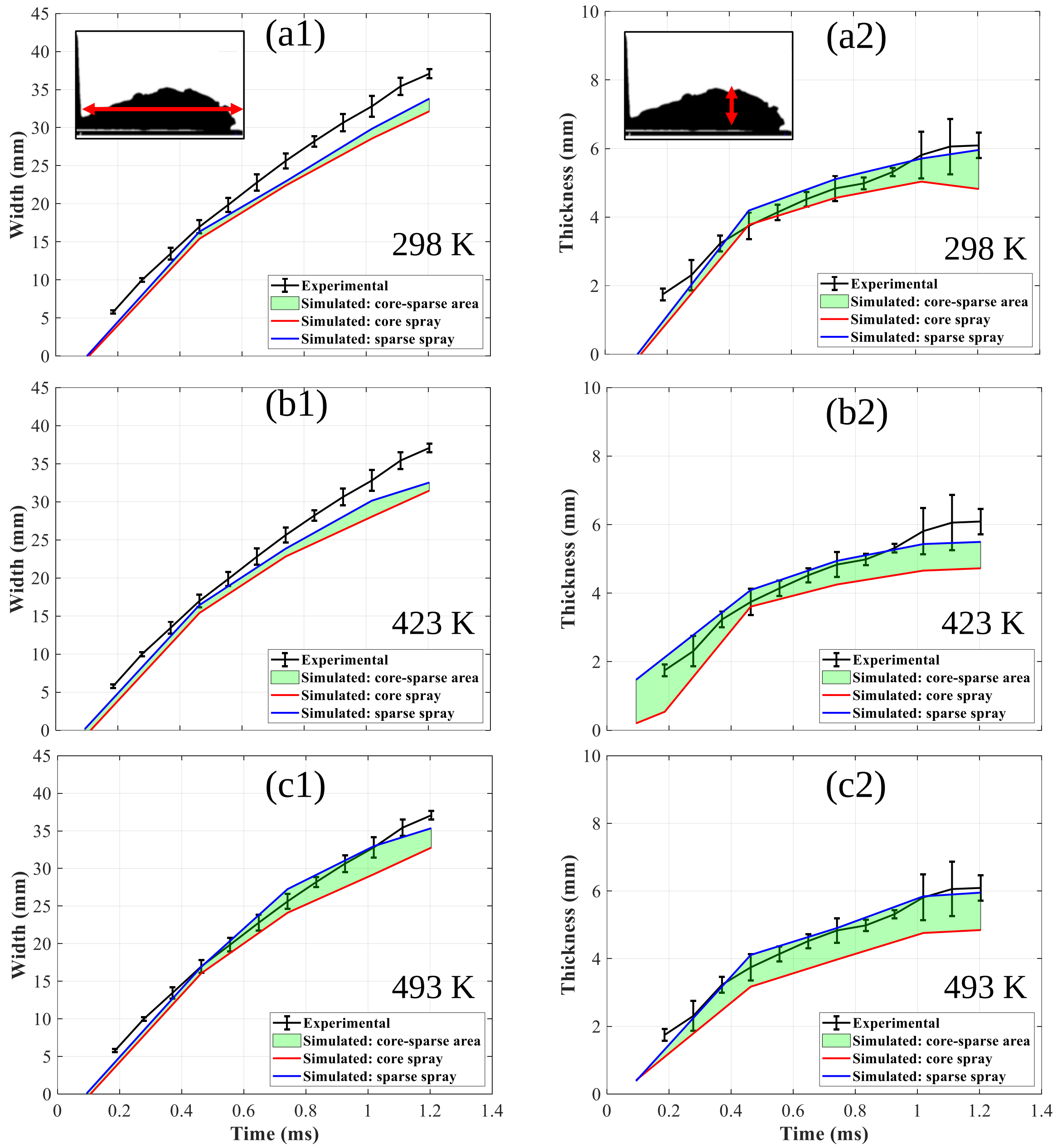

Figure B-1: Comparison between width and thickness of the rebounded cloud for a distance of 30 mm between the injector tip and the heated plate and an injection pressure of 500 bar (a1 and b1: 298 K; b1 and b2: 423 K; c1 and c2: 493 K).

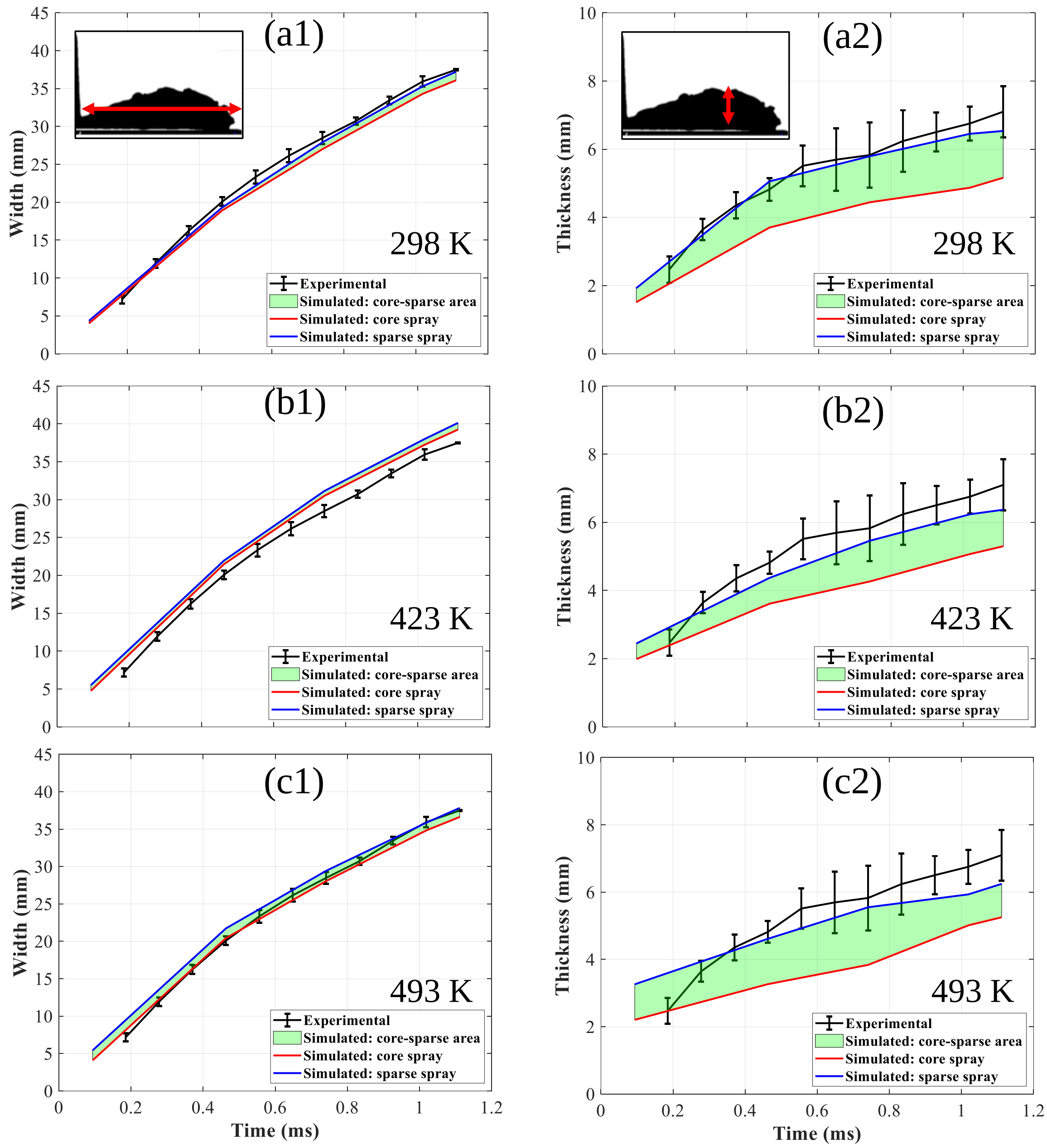

FigureB-2: Comparison between width and thickness of the rebounded cloud for a distance of 30 mm between the injector tip and the heated plate and an injection pressure of 700 bar (a1 and b1: 298 K; b1 and b2: 423 K; c1 and c2: 493 K).

Appendix C

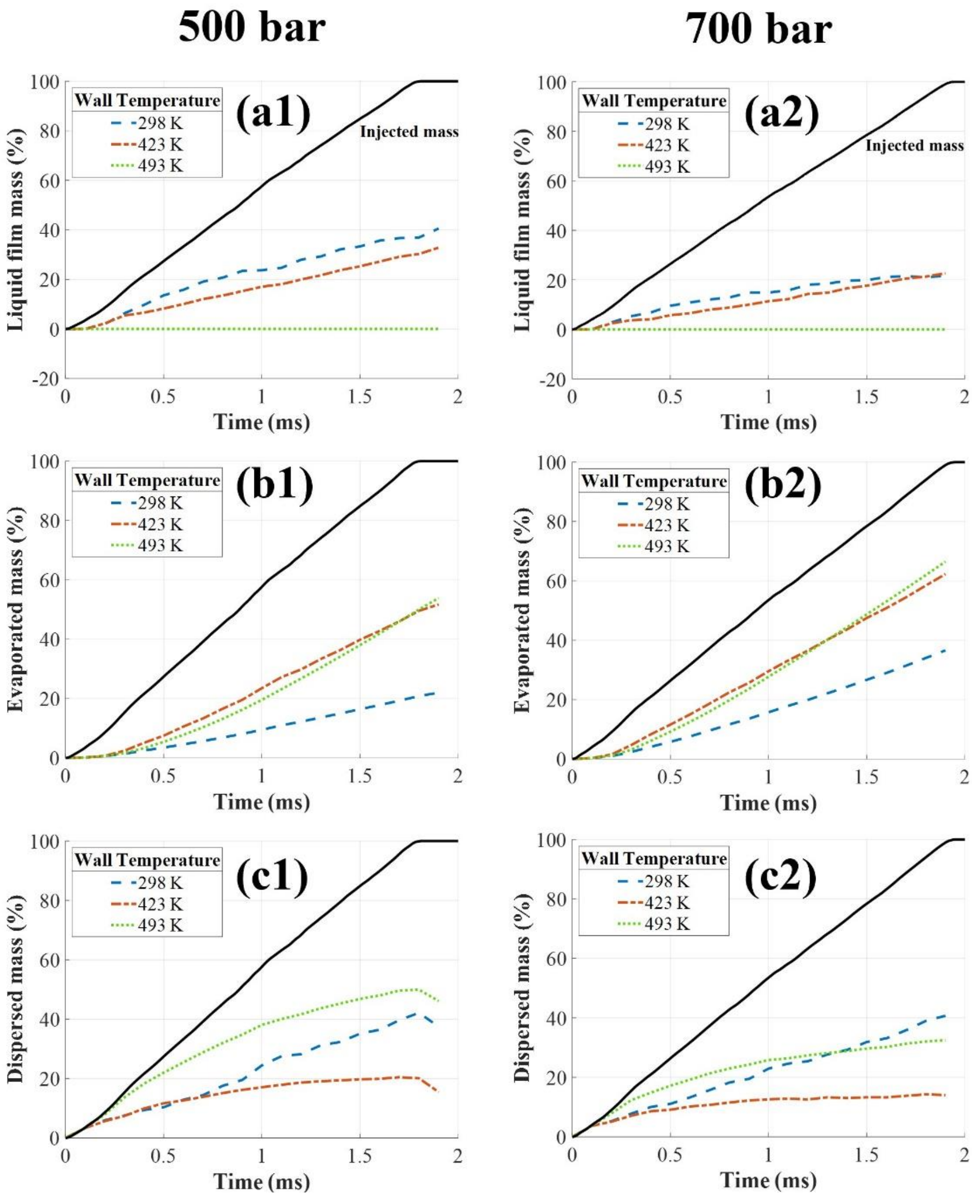

Figure C-1: Comparison of the trends of liquid film (a1, a2), evaporated (b1, b2) and dispersed masses (c1, c2) for the distance of 30 mm between the injector and the plate.